Supporting Information

0D Hybrid Indium Halide as Highly Efficient X-ray Scintillation and Ultra-Sensitive Fluorescence Probe

Dong-Yang Li,[ab] Yan-Bing Shang,[a] Qi Liu,[a] Hua-Wu Zhang,[a] Xin-Yue Zhang,[a] Cheng-Yang Yue[a]*, Xiao-Wu Lei[a]*

[a] *School of Chemistry, Chemical Engineer and Materials, Jining University, Qufu, Shandong, 273155, P. R. China*

[b] *School of Chemistry and Chemical Engineering, Qufu Normal University, Qufu, Shandong, 273165, P. R. China*

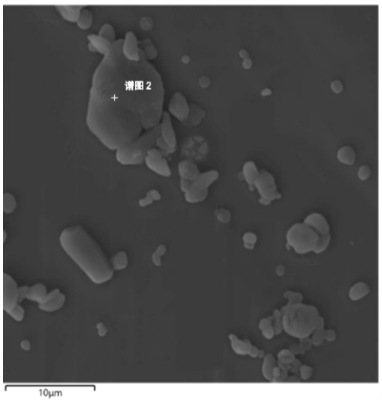

(a)

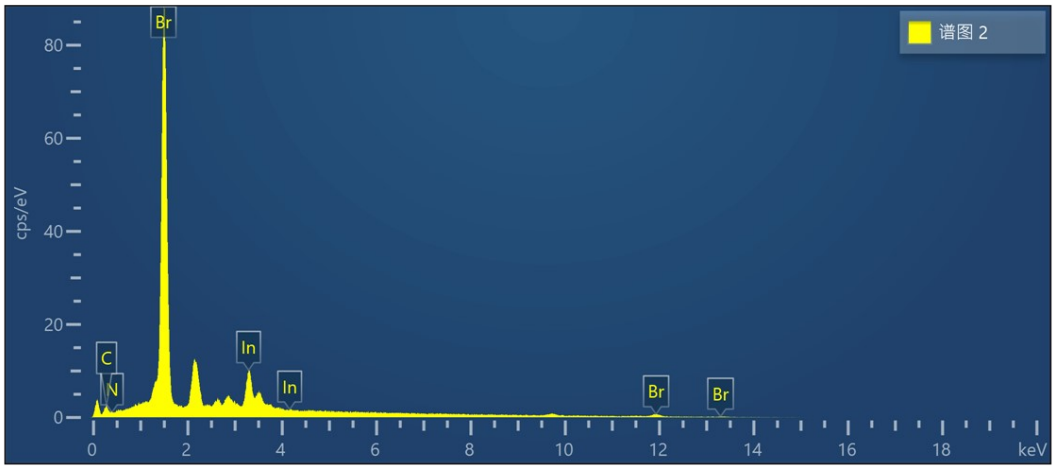

(b)

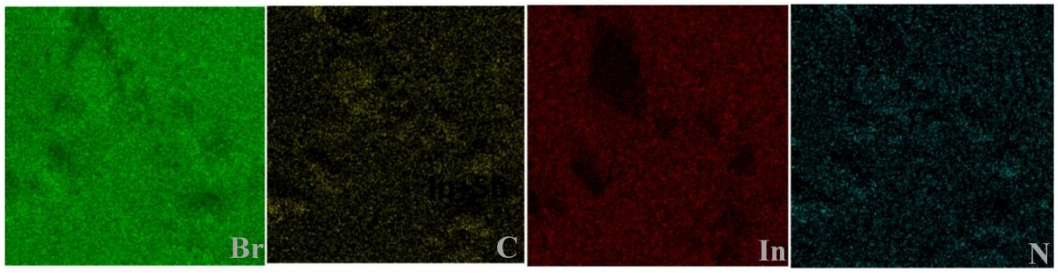

(c)

Fig. S1 SEM photo image (a), EDS result (b) and elemental mapping (c) of [DADPA]$InBr_6 \cdot H_2O$ bulk crystal.

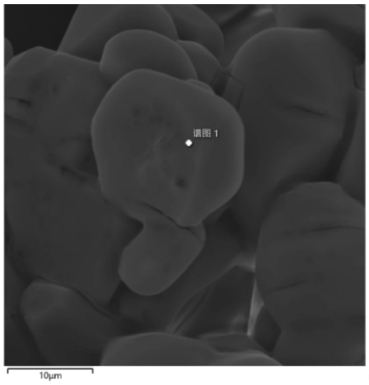

(a)

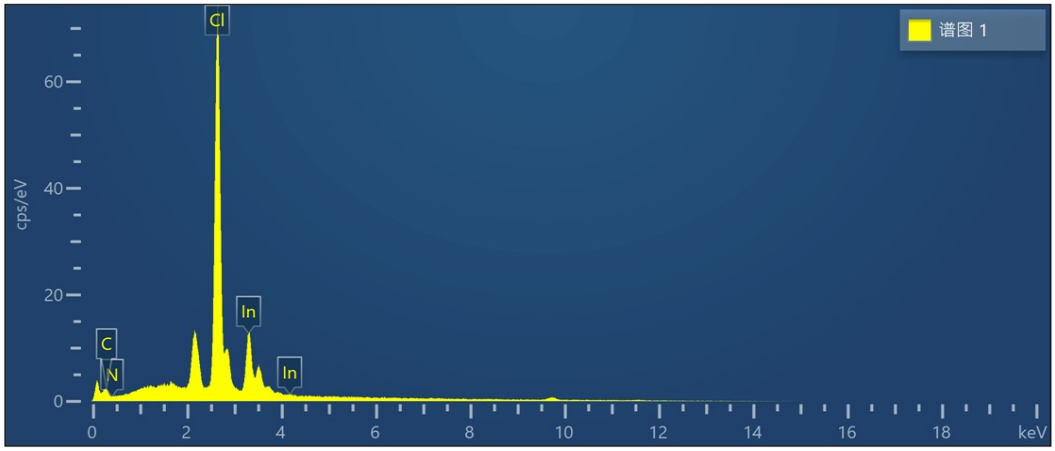

(b)

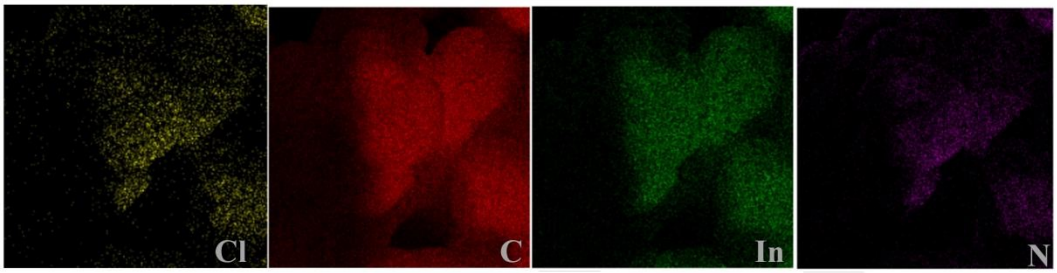

(c)

Fig. S2 SEM photo image (a), EDS result (b) and elemental mapping (c) of [DADPA]$InCl_6 \cdot H_2O$ bulk crystal.

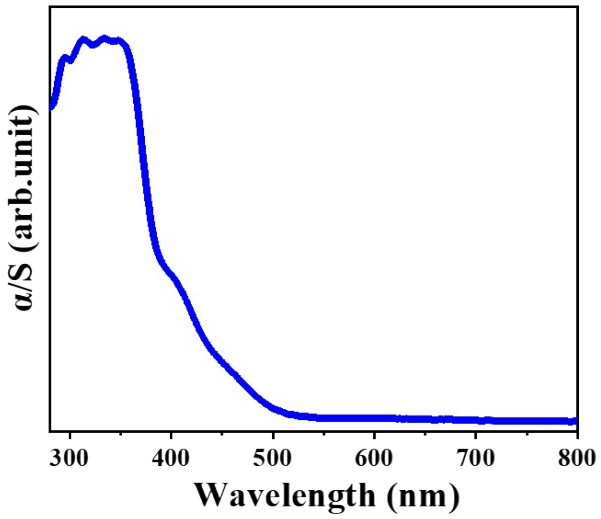

Fig. S3 UV-vis absorption spectra of [DADPA]$InBr_6 \cdot H_2O$.

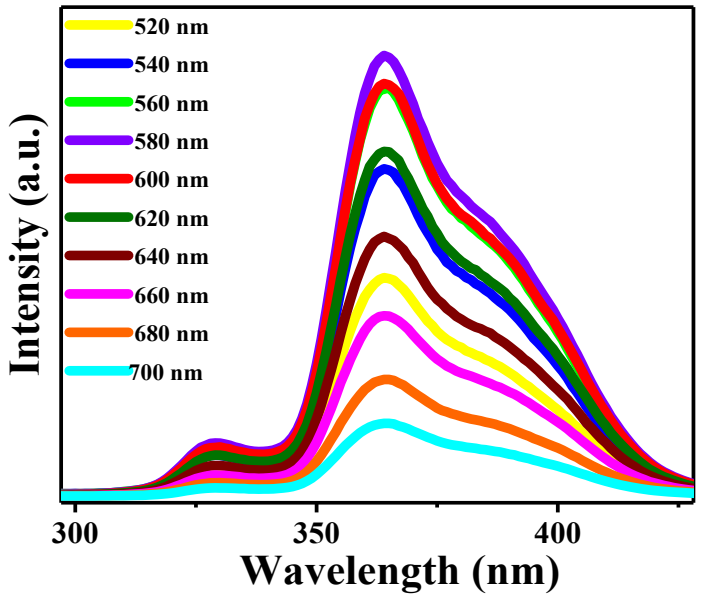

(a)

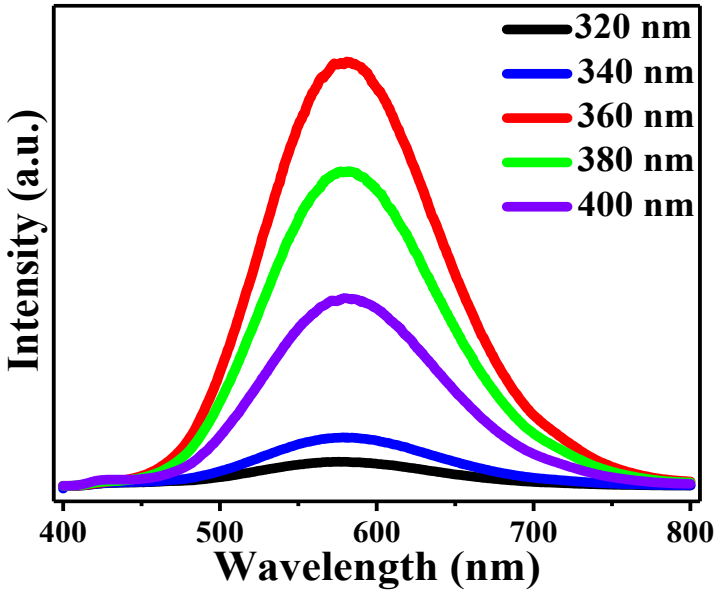

(b)

Fig. S4 Emission wavelength dependent excitation spectra (a) and excitation wavelength dependent emission spectra (b) of [DADPA]$InBr_6 \cdot H_2O$.

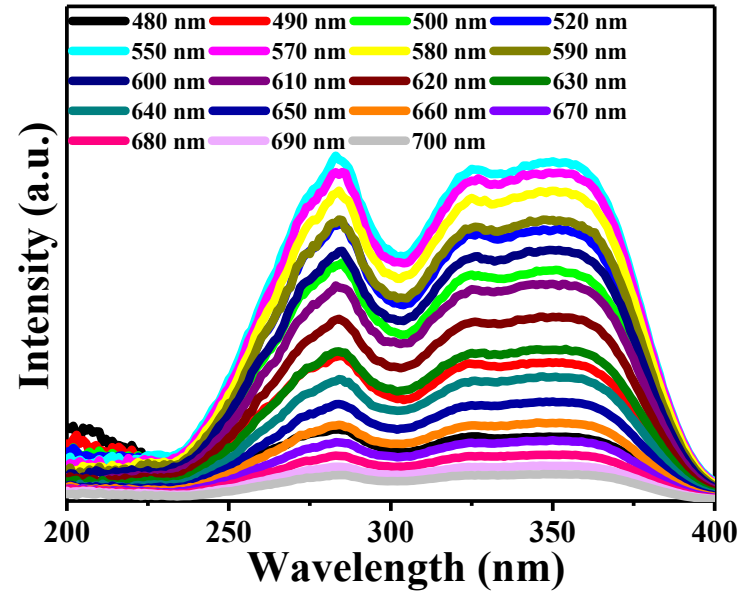

(a)

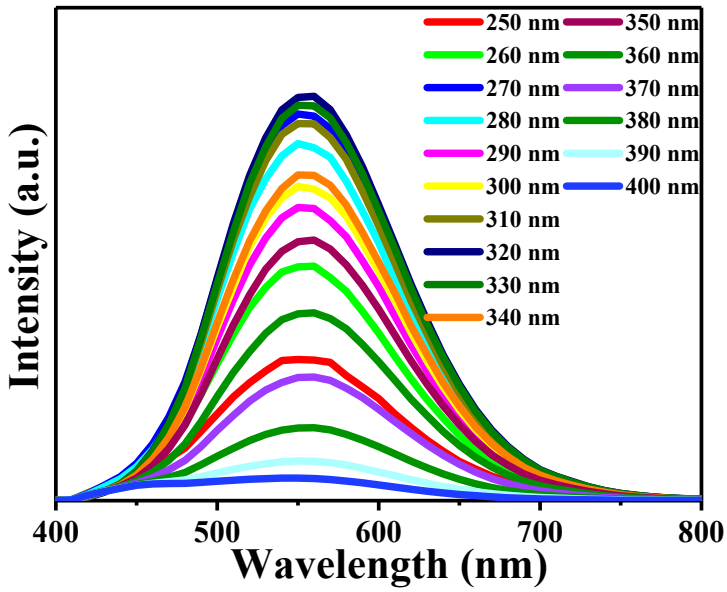

(b)

Fig. S5 Emission wavelength dependent excitation spectrum (a) and excitation wavelength dependent emission spectrum (b) of $[DADPA]InCl_6 \cdot H_2O$.

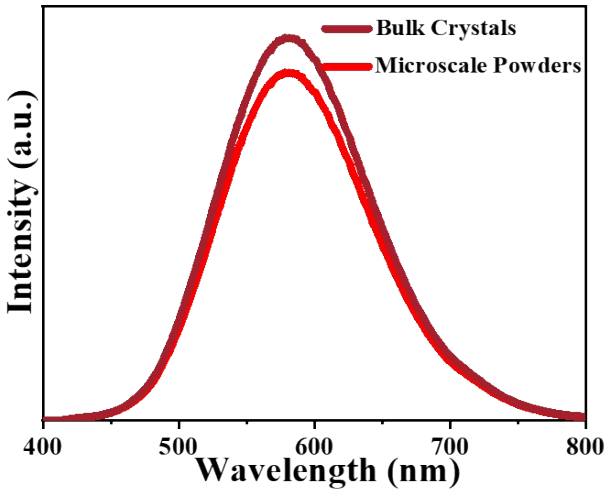

(a)

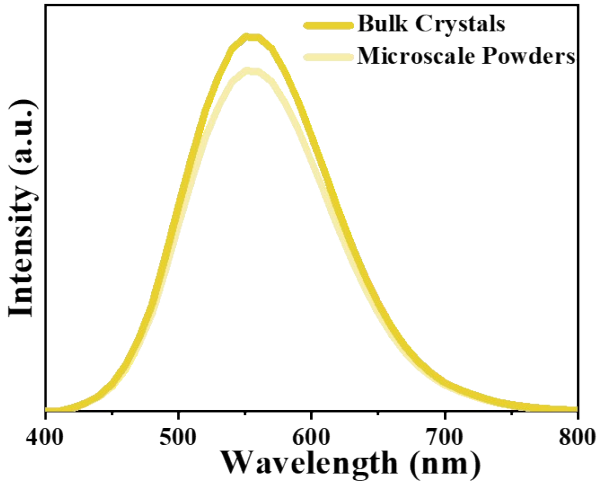

(b)

Fig. S6 Comparisons of PL emission spectra of bulk crystals and microscale powders of [DADPA]$InBr_6 \cdot H_2O$ (a) and [DADPA]$InCl_6 \cdot H_2O$ (b).

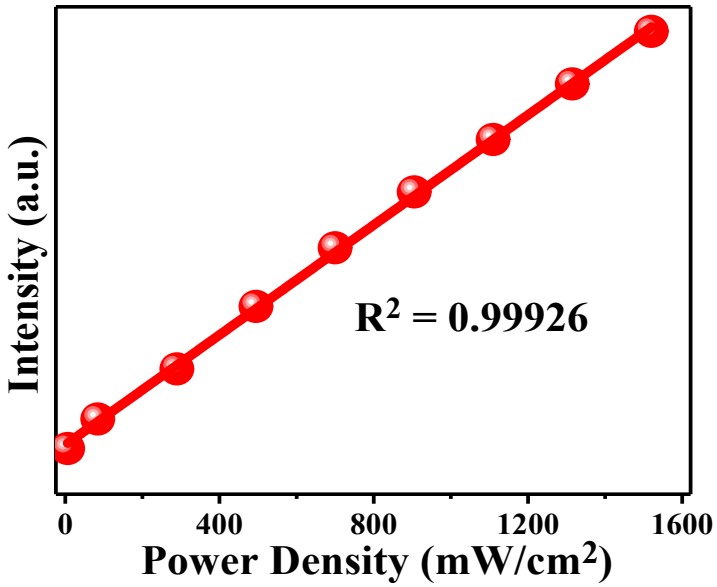

(a)

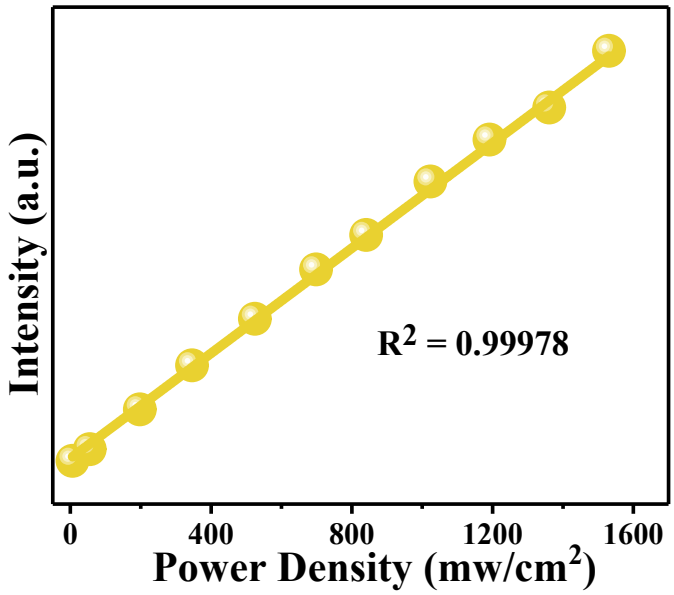

(b)

Fig. S7 Excitation power density dependent PL emission intensities of [DADPA]$InBr_6 \cdot H_2O$ (a) and [DADPA]$InCl_6 \cdot H_2O$ (b).

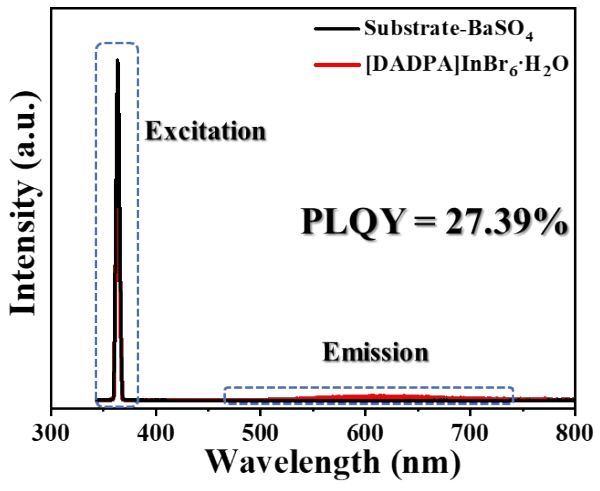

(a)

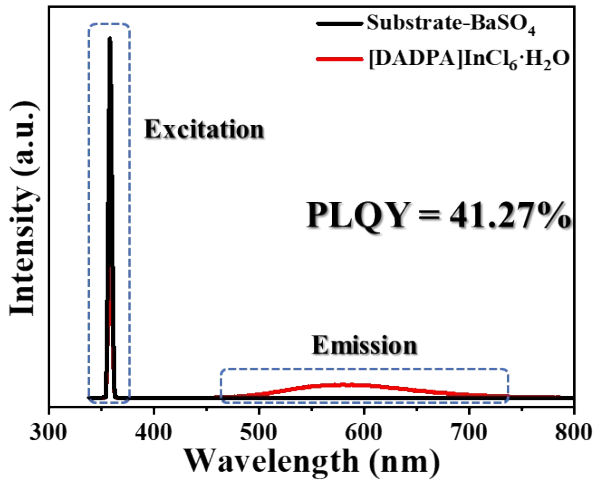

(b)

Fig. S8 The absolute PLQY of $[DADPA]InBr_6 \cdot H_2O$ (a) and $[DADPA]InCl_6 \cdot H_2O$ (b).

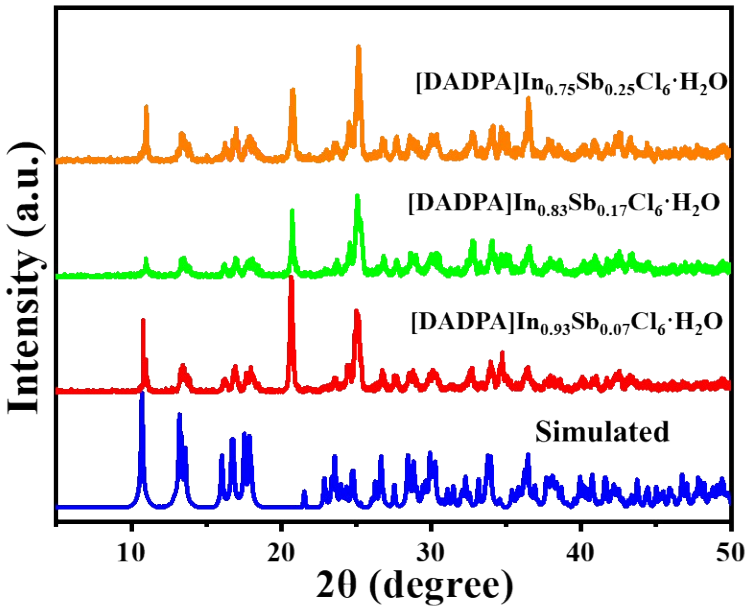

Fig. S9 Experimental PXRD pattern and simulated data of $[DADPA]In_{1-x}Sb_xCl_6 \cdot H_2O$.

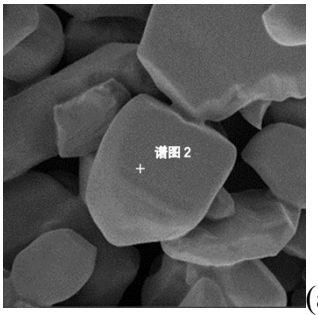

(a)

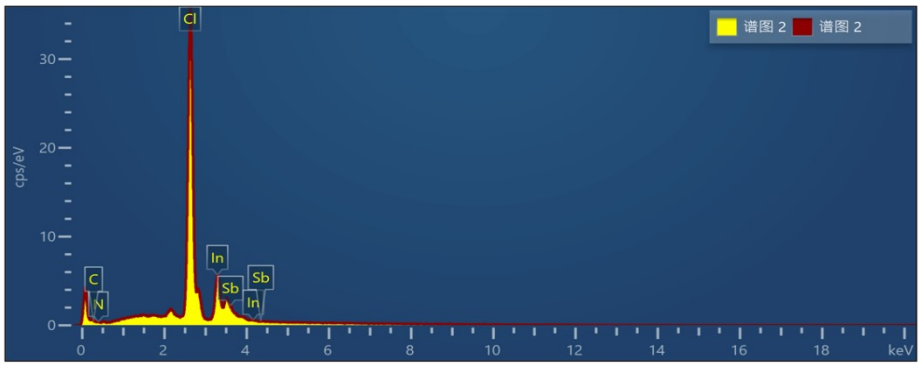

(b)

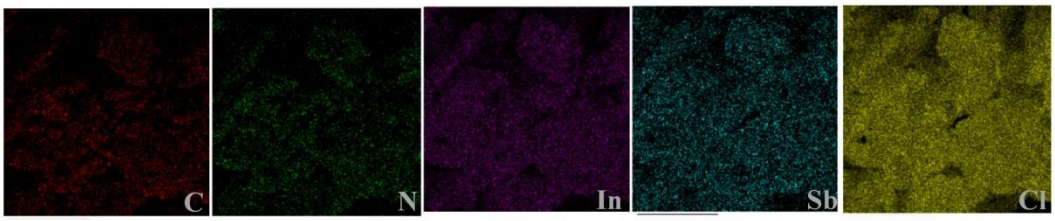

(c)

Fig. S10 SEM photo image (a), EDS result (b) and elemental mapping (c) of [DADPA]$In_{0.83}Sb_{0.17}Cl_6 \cdot H_2O$ bulk crystal.

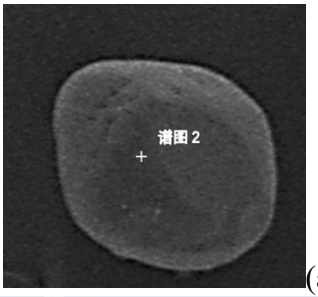

(a)

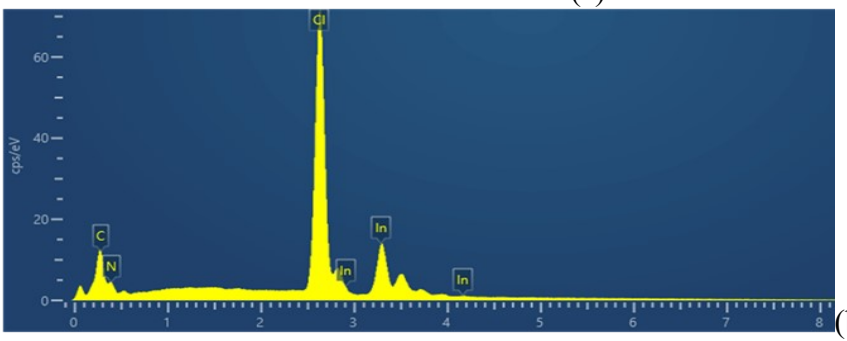

(b)

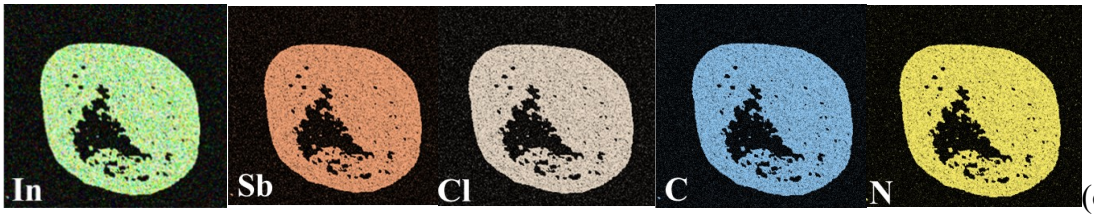

(c)

Fig. S11 SEM photo image (a), EDS result (b) and elemental mapping (c) of [DADPA]$In_{0.93}Sb_{0.07}Cl_6 \cdot H_2O$ bulk crystal.

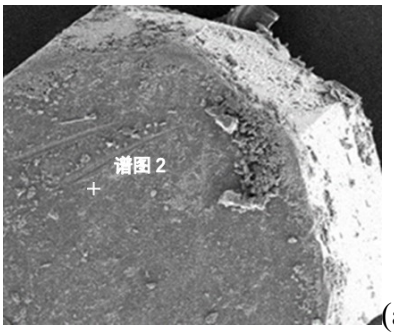

(a)

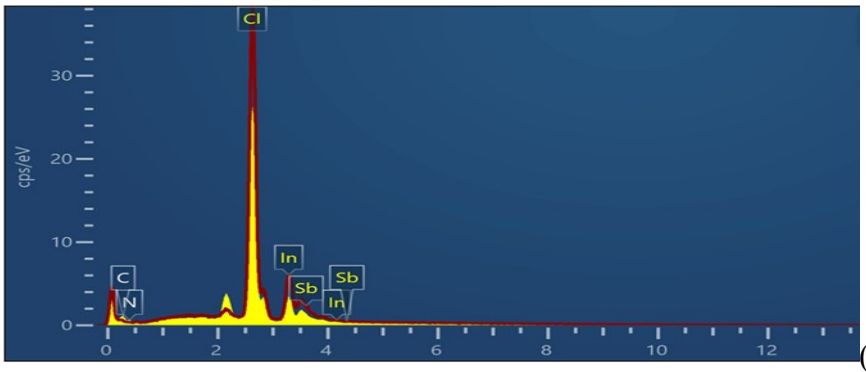

(b)

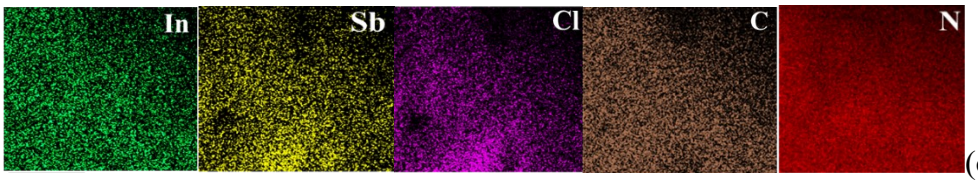

(c)

Fig. S12 SEM photo image (a), EDS result (b) and elemental mapping (c) of [DADPA]$In_{0.75}Sb_{0.25}Cl_6 \cdot H_2O$ bulk crystal.

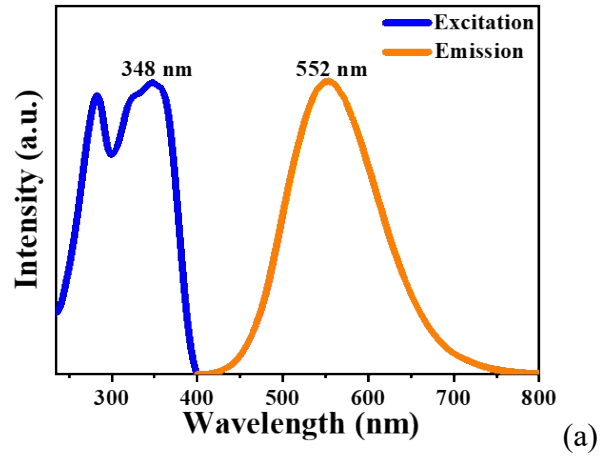

(a)

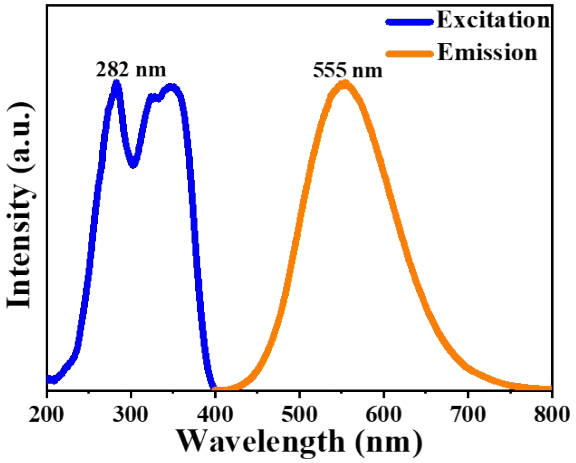

(b)

Fig. S13 The PL excitation and emission spectra of [DADPA]$In_{0.93}Sb_{0.07}Cl_6 \cdot H_2O$ (a) and [DADPA]$In_{0.75}Sb_{0.25}Cl_6 \cdot H_2O$ (b).

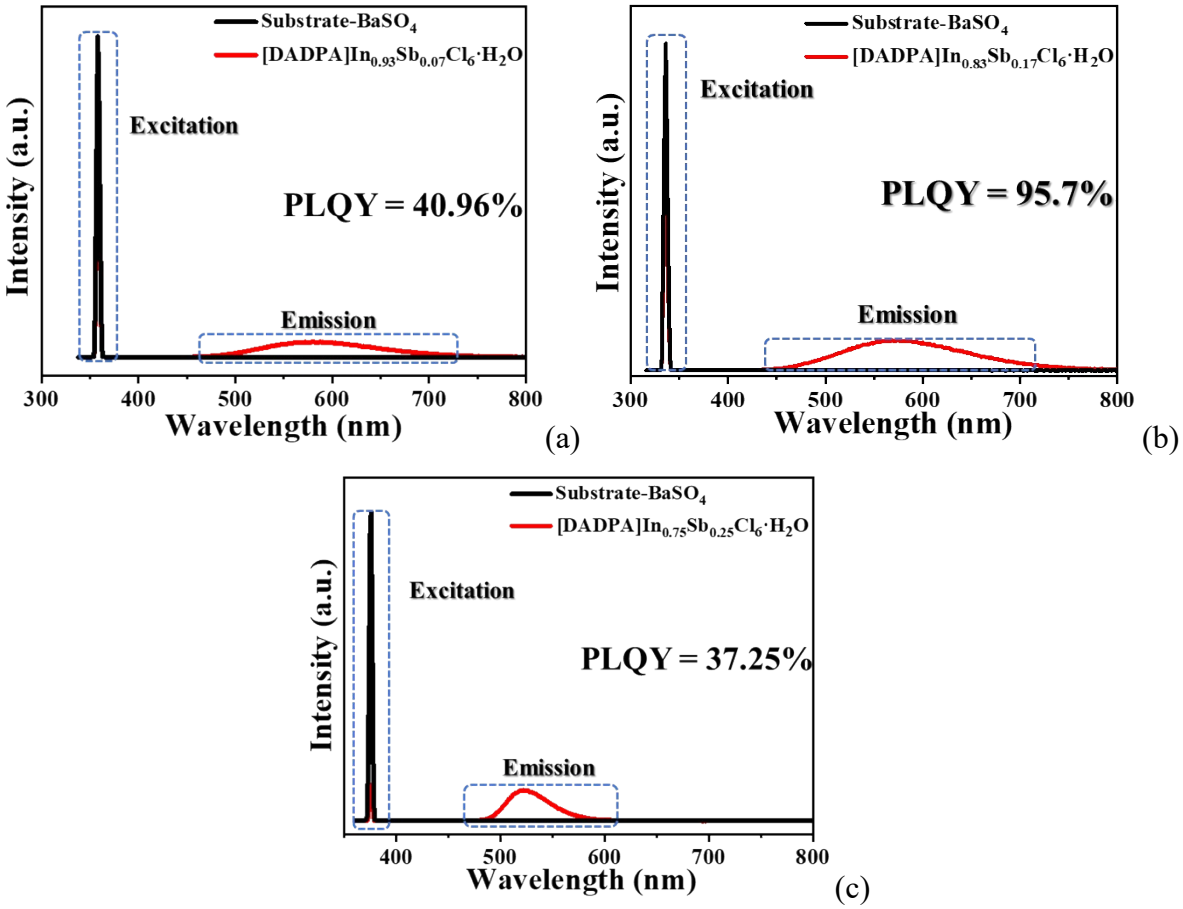

Fig. S14 PLQYs of $[DADPA]In_{0.93}Sb_{0.07}Cl_6 \cdot H_2O$ (a), $[DADPA]In_{0.83}Sb_{0.17}Cl_6 \cdot H_2O$ (b) and $[DADPA]In_{0.75}Sb_{0.25}Cl_6 \cdot H_2O$ (c).

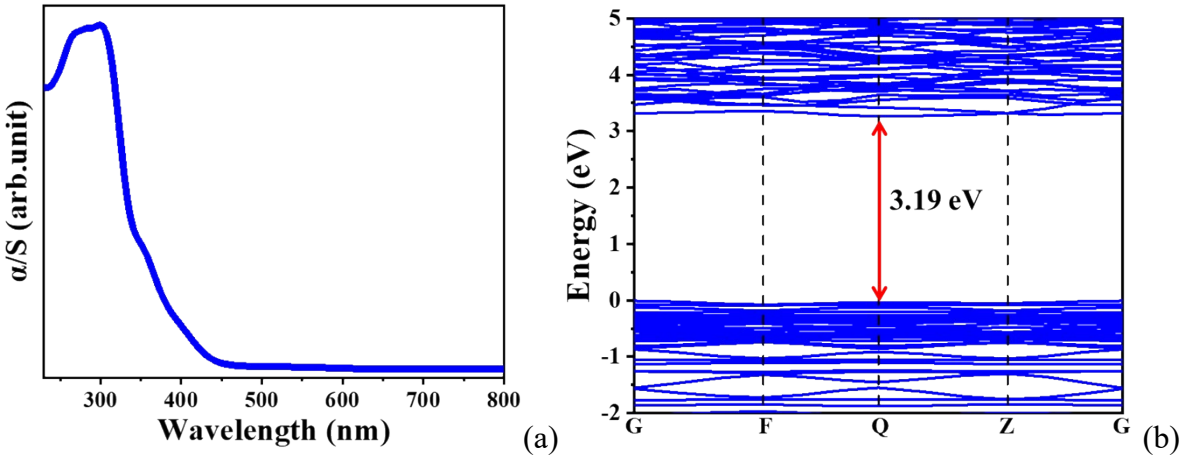

Fig. S15 The UV-vis absorption spectrum (a) and calculated band structure (b) of $[DADPA]In_{0.93}Sb_{0.07}Cl_6 \cdot H_2O$.

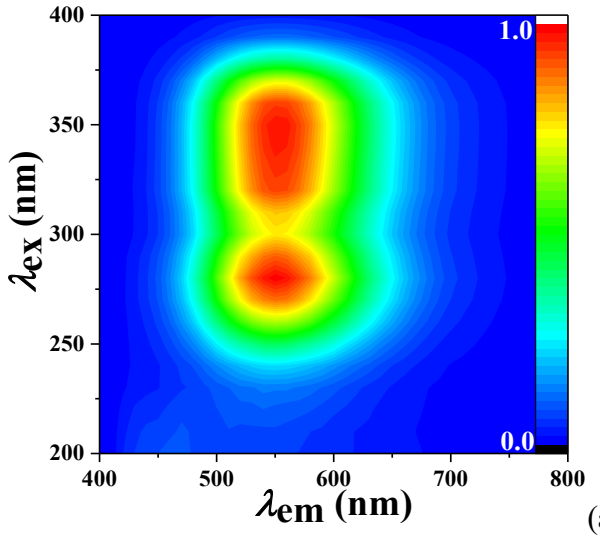

(a)

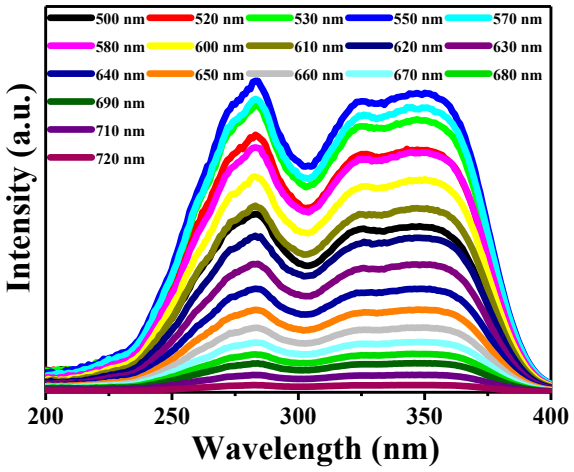

(b)

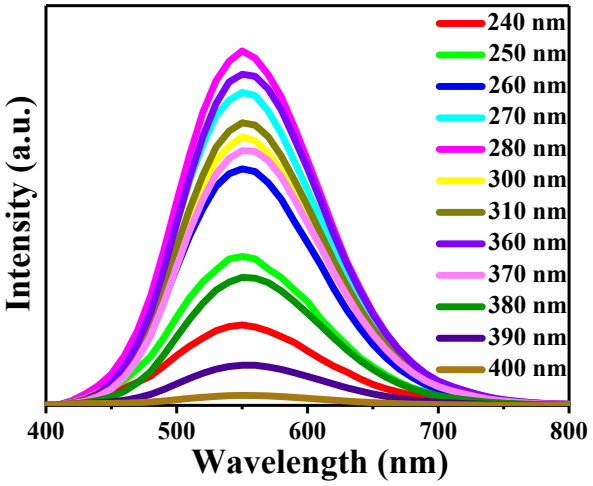

(c)

Fig. S16 3D consecutive PL excitation and emission map (a), emission wavelength dependent excitation spectra (b) and excitation dependent emission spectra (c) of [DADPA]$In_{0.83}Sb_{0.17}Cl_6 \cdot H_2O$.

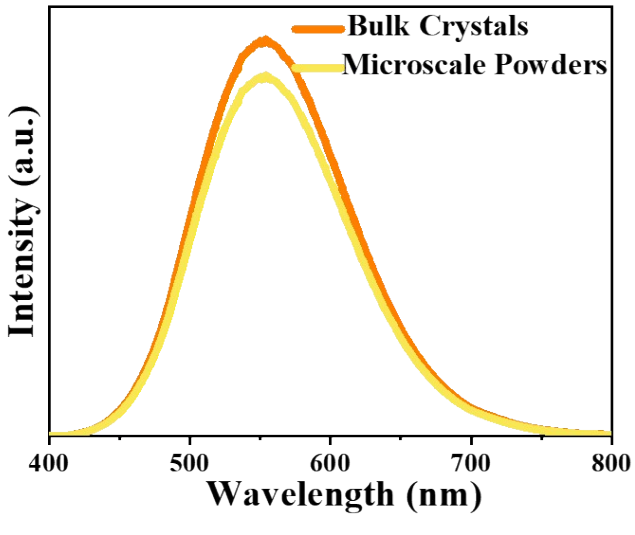

(a)

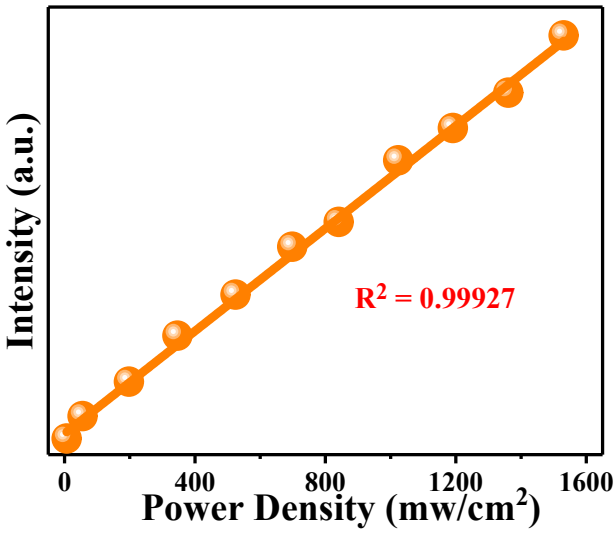

(b)

Fig. S17 Comparisons of PL emission spectra of bulk crystals and microscale powders (a), excitation power density dependent PL emission intensity (b) of [DADPA]$In_{0.83}Sb_{0.17}Cl_6 \cdot H_2O$.

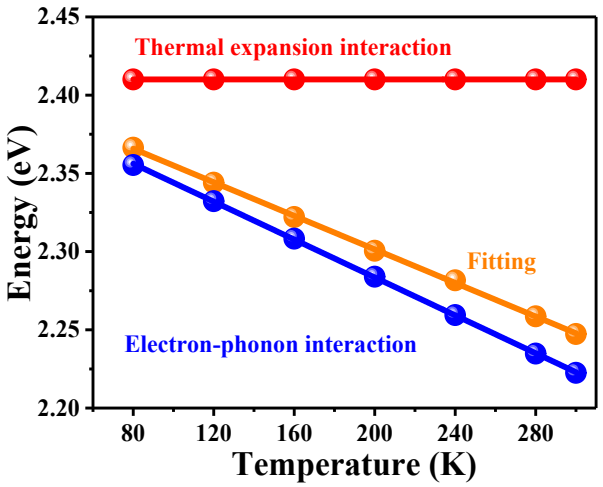

Fig. S18 Temperature-dependent PL energy evolution with the contribution of thermal expansion and electronic–phonon interactions of [DADPA]$In_{0.83}Sb_{0.17}Cl_6 \cdot H_2O$.

Note: By using the oneoscillator model and assuming a linear relationship between thermal expansion and temperature, the temperature-dependent PL emission energy evolution is fitted by the follow equation:

$$E_g(T) = E_0 + A_{TE}T + A_{EP}\left[\frac{2}{\exp\left(\frac{h_w}{K_B T}\right) - 1} + 1\right]$$

where E_0 is the unrenormalized band gap, $E_g(T = 0) = E_0 + A_{EP}$; A_{TE} and A_{EP} are the weight of TE and EP interactions, respectively; h_ω is the average optical phonon energy; and k_B is Boltzmann's constant. The fitted parameters are: E_0 = 2.41 eV, A_{TE} = 0.054 meV K^{-1}, A_{EP} = −28.6 meV, and h_ω = 8 meV. The contributions of thermal expansion and electronic–phonon interactions are defined as [E_{TE}(300 K)-E_{TE}(80 K)] and [E_{EP}(300 K)-E_{EP}(80 K)] with values of 35.9 and -60.2 meV, respectively. Notably, the absolute magnitude of Δ_{EP} is ≈1.67 times of that from Δ_{TE}, which demonstrates that the EP interactions play a more dominant role in determining the temperature-responsive emission over the TE effect. As a result, the TE induced linear widening of bandgap can be fully compensated and reversed by the EP interactions upon heating, and the sublinear trend of band gap with temperature increasing is mainly determined by the EP interaction. Specifically, EP interaction enhance with increasing temperature, which leads to the narrowing of energy gap between conducting and valence band, consequently reducing the emission energy and resulting in the red-shift of emission

wavelength.

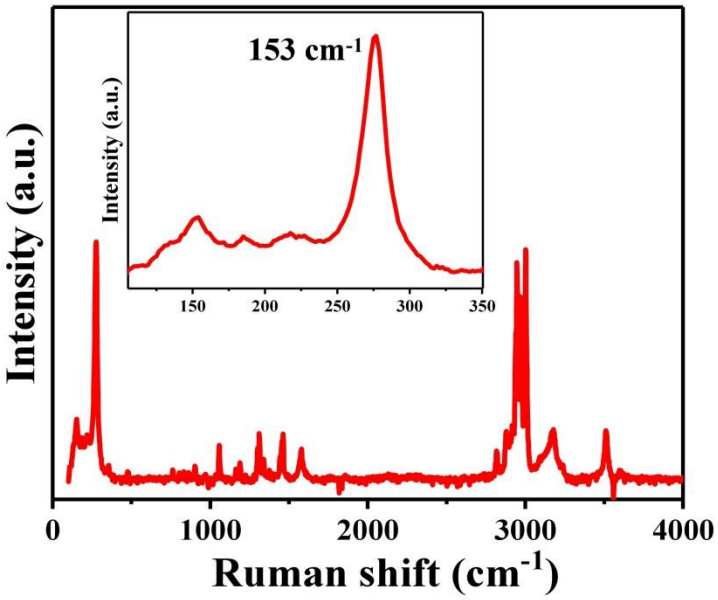

Fig. S19 Raman spectrum of [DADPA]$In_{0.83}Sb_{0.17}Cl_6 \cdot H_2O$.

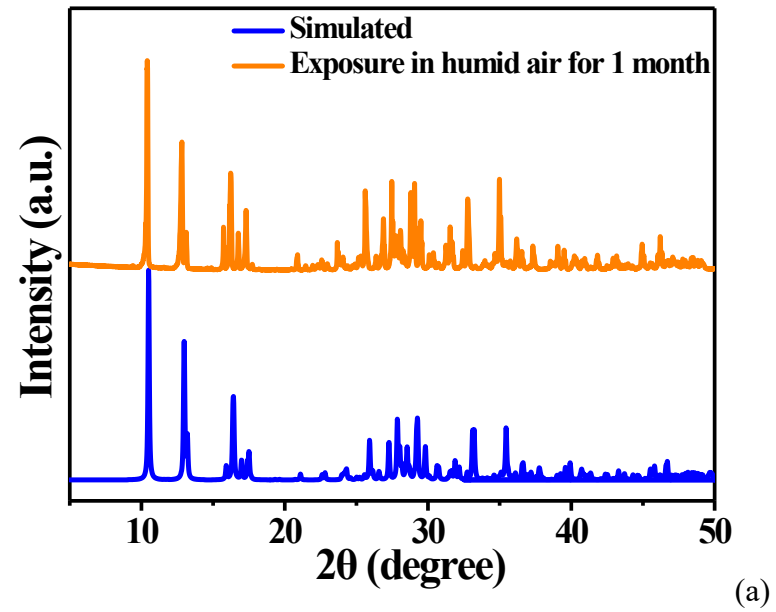

(a)

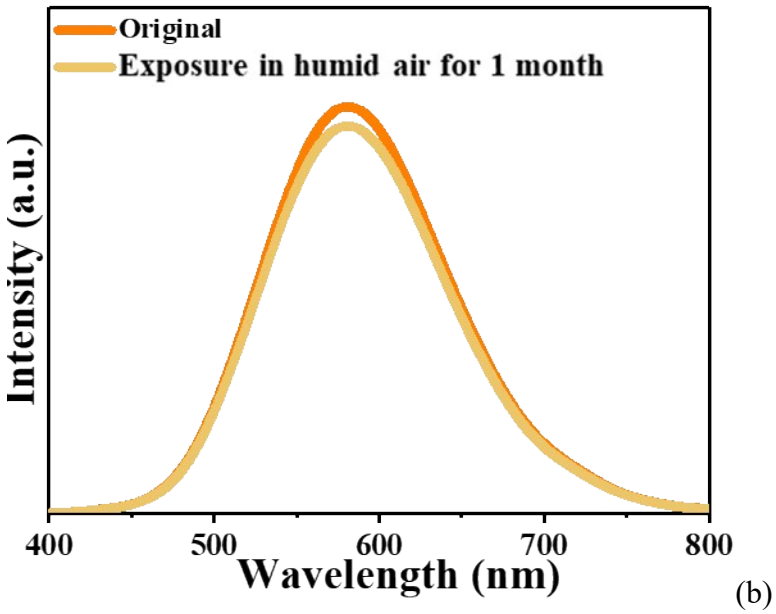

(b)

Fig. S20 The experimental PXRD pattern (a) and PL emission spectra (b) of [DADPA]$In_{0.83}Sb_{0.17}Cl_6 \cdot H_2O$ after exposure in humid air for one month.

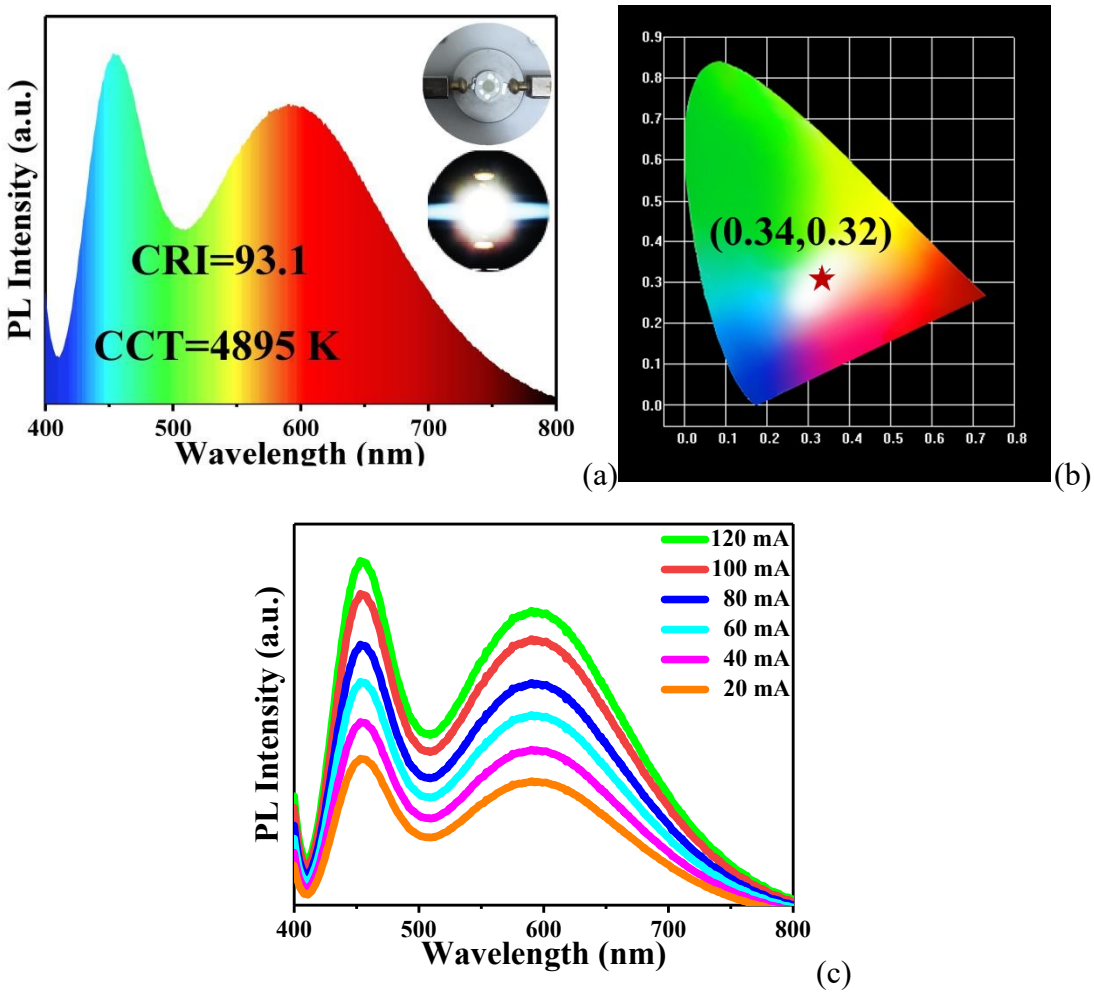

Fig. S21 Characterizations of fabricated white LED based on [DADPA]$In_{0.83}Sb_{0.17}Cl_6 \cdot H_2O$: a) The EL emission spectrum at 20 mA drive current (inset: photographs of fabricated white LED before and after switching power supply); b) CIE chromaticity coordinates; c) Drive current dependent PL emission spectra.

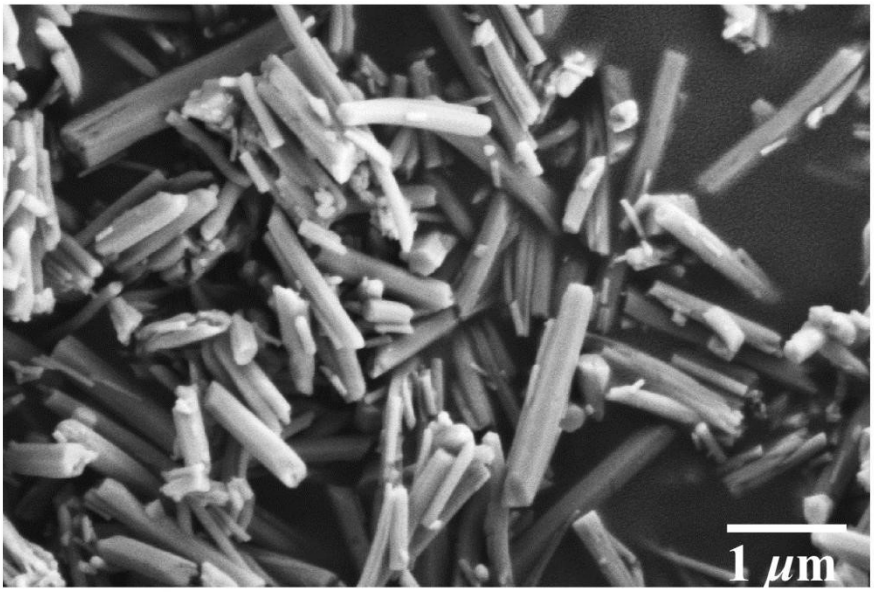

Fig. S22 SEM photo image of [DADPA]$In_{0.83}Sb_{0.17}Cl_6 \cdot H_2O$ microcrystals.

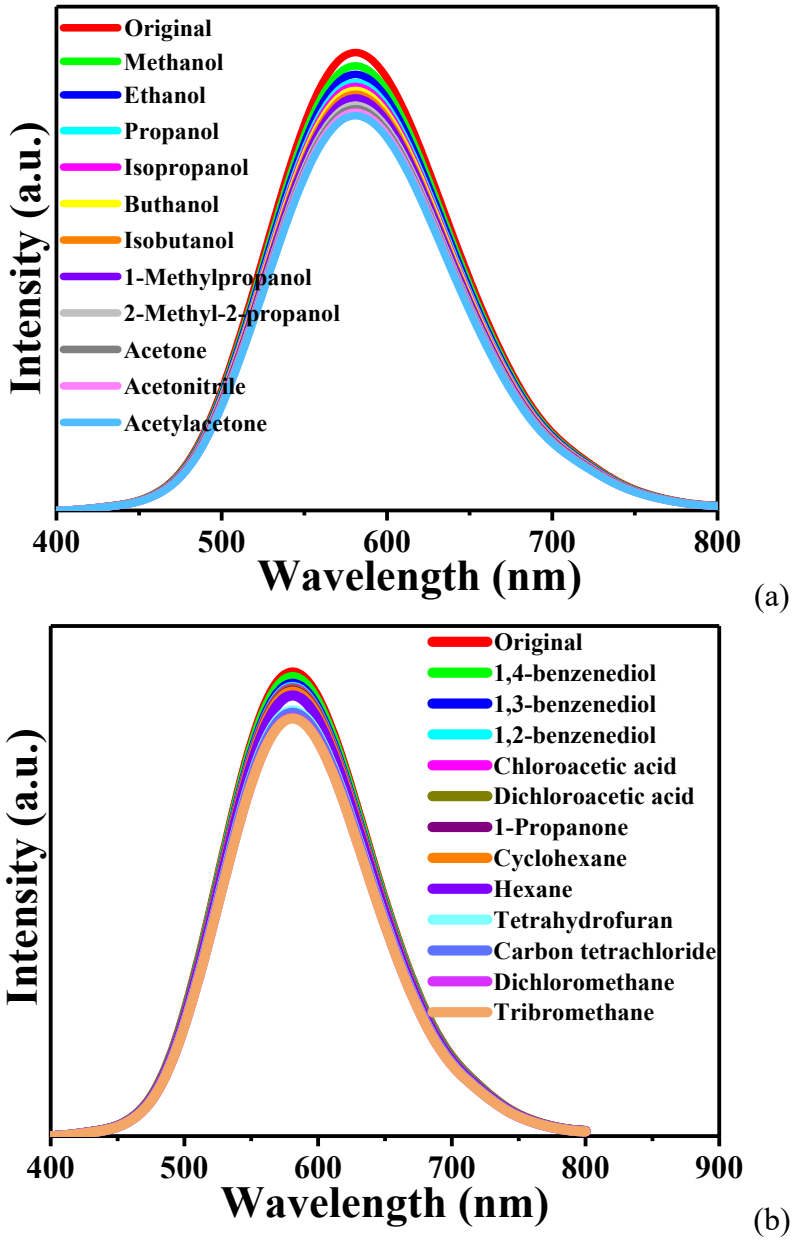

Fig. S23 The PL emission spectra of [DADPA]$In_{0.83}Sb_{0.17}Cl_6 \cdot H_2O$ microcrystals toward various organic solvents.

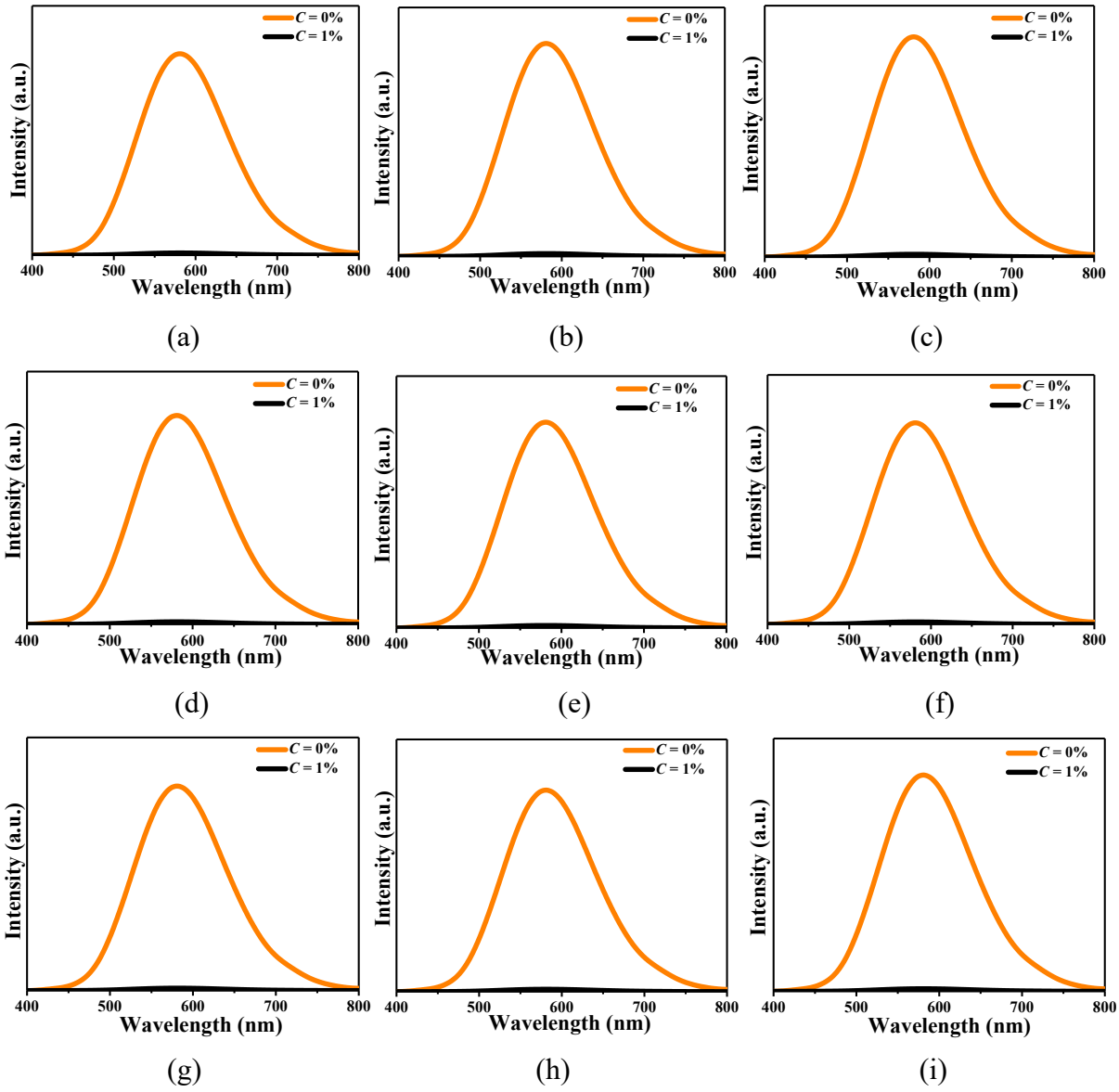

Fig. S24 PL emission spectra (a-i) of [DADPA]$In_{0.83}Sb_{0.17}Cl_6 \cdot H_2O$ microcrystals toward nitrobenzene ($C_6H_5NO_2$) solutions in various organic solvents with concentrations of 0% and 1% including benzene (C_6H_6) (a), dimethylbenzene ($C_6H_5(CH_3)_2$) (b), ethylbenzene ($C_6H_5C_2H_5$) (c), vinylbenzene ($C_6H_5CHCH_2$) (d), methoxybenzene ($C_6H_5OCH_3$) (e), fluorobenzene (C_6H_5F) (f), chlorobenzene (C_6H_5Cl) (g), bromobenzene (C_6H_5Br) (h) and iodobenzene (C_6H_5I) (i).

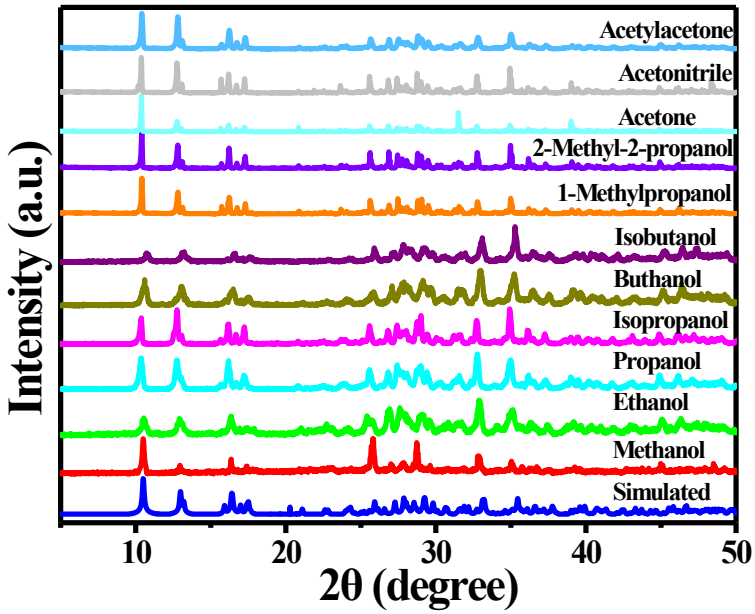

Fig. S25 The experimental PXRD patterns of [DADPA]$In_{0.83}Sb_{0.17}Cl_6 \cdot H_2O$ microcrystals after soaking in various organic solvents.

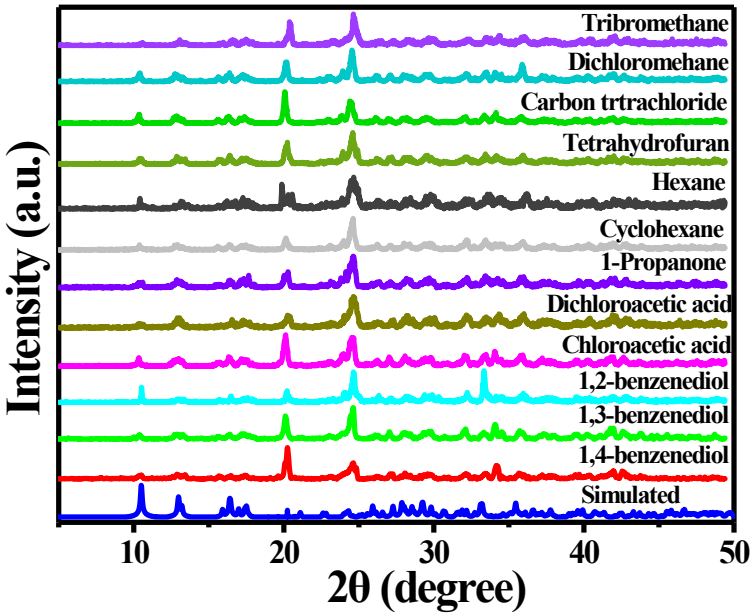

Fig. S26 The experimental PXRD patterns of [DADPA]$In_{0.83}Sb_{0.17}Cl_6 \cdot H_2O$ microcrystals after soaking in various organic solvents.

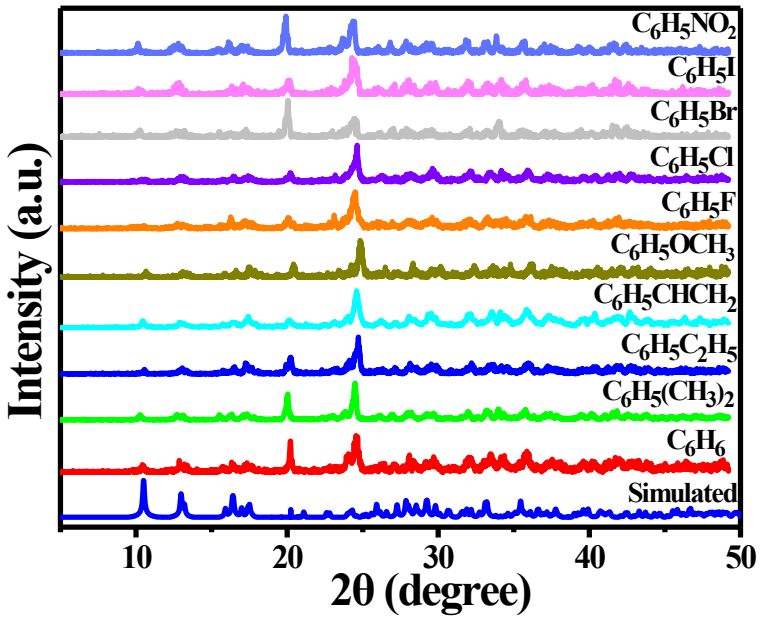

Fig. S27 The experimental PXRD patterns of $[DADPA]In_{0.83}Sb_{0.17}Cl_6 \cdot H_2O$ microcrystals after soaking in various organic solvents including benzene (C_6H_6), dimethylbenzene ($C_6H_5(CH_3)_2$), ethylbenzene ($C_6H_5C_2H_5$), vinylbenzene ($C_6H_5CHCH_2$), methoxybenzene ($C_6H_5OCH_3$), fluorobenzene (C_6H_5F), chlorobenzene (C_6H_5Cl), bromobenzene (C_6H_5Br), iodobenzene (C_6H_5I) and nitrobenzene ($C_6H_5NO_2$).

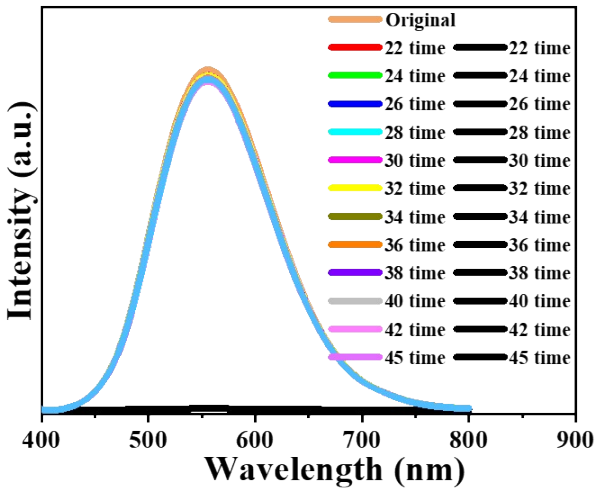

Fig. S28 PL emission spectra during the consecutive quenching-recovering cycles in $C_6H_5NO_2$ as a function of cycle number.

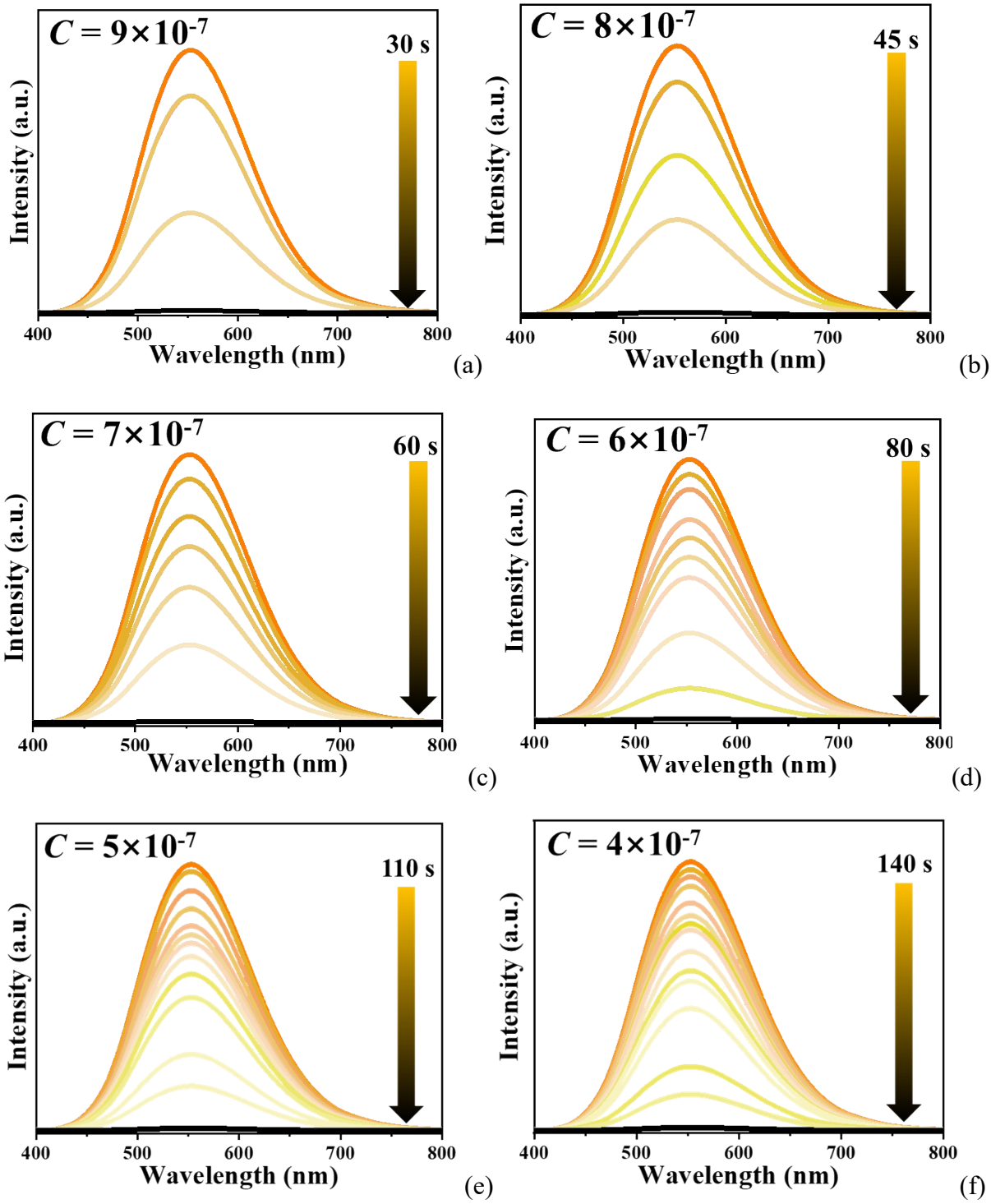

Fig. S29 Soaking time-dependent PL emission spectral evolutions of [DADPA]$In_{0.83}Sb_{0.17}Cl_6 \cdot H_2O$ microcrystals in mixed $C_6H_5NO_2/C_6H_6$ solutions with different concentrations of 9×10^{-7} (a), 8×10^{-7} (b), 7×10^{-7} (c), 6×10^{-7} (d), 5×10^{-7} (e), 4×10^{-7} (f).

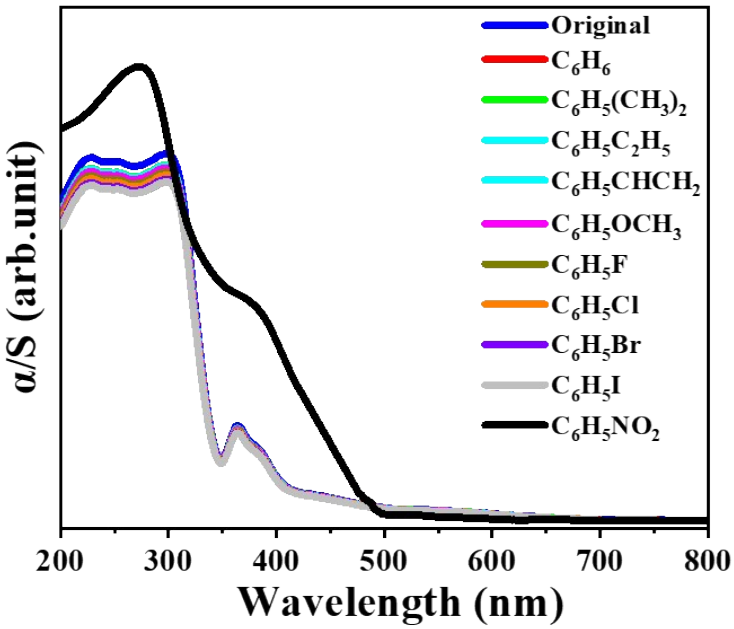

Fig. S30 UV-vis absorption spectra of [DADPA]$In_{0.83}Sb_{0.17}Cl_6 \cdot H_2O$ microcrystals after soaking in various organic solvents including benzene (C_6H_6), dimethylbenzene ($C_6H_5(CH_3)_2$), ethylbenzene ($C_6H_5C_2H_5$), vinylbenzene ($C_6H_5CHCH_2$), methoxybenzene ($C_6H_5OCH_3$), fluorobenzene (C_6H_5F), chlorobenzene (C_6H_5Cl), bromobenzene (C_6H_5Br), iodobenzene (C_6H_5I) and nitrobenzene ($C_6H_5NO_2$).

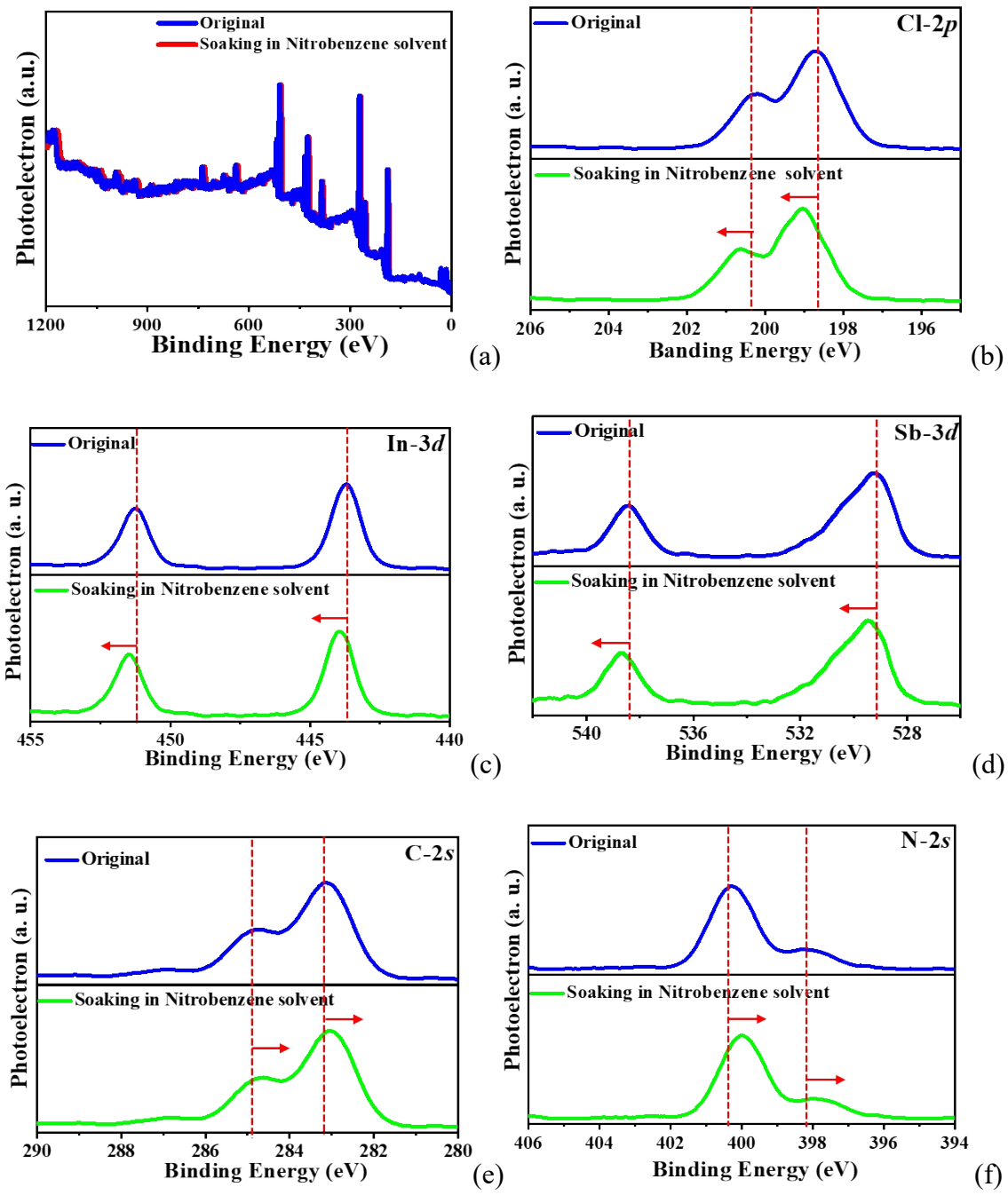

Fig. S31 The XPS spectra of [DADPA]$In_{0.83}Sb_{0.17}Cl_6 \cdot H_2O$ microcrystals after soaking in nitrobenzene ($C_6H_5NO_2$).

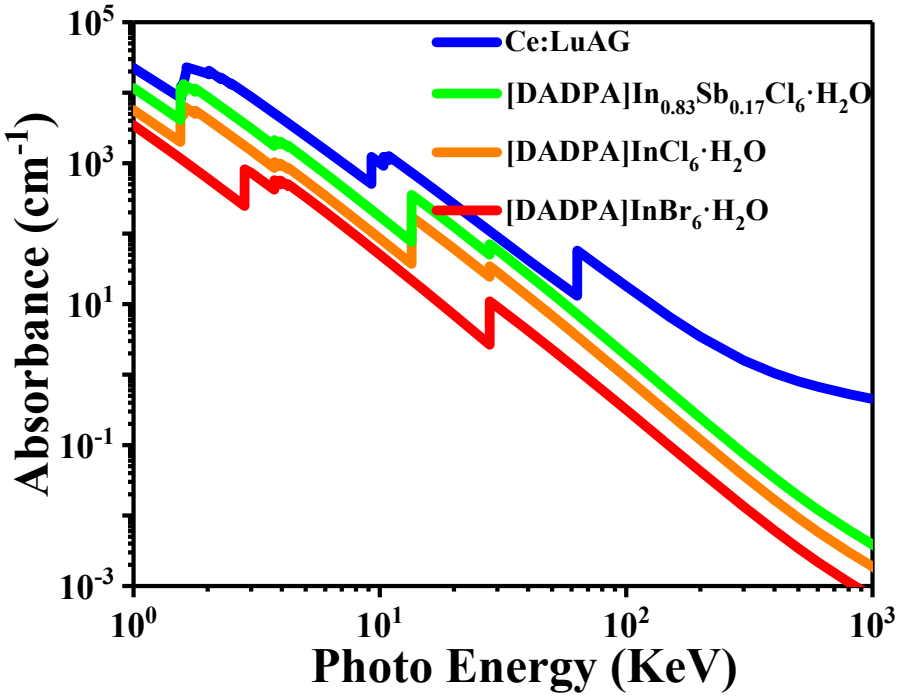

Fig. S32 Absorption coefficients as a function of photon energy from 1 KeV to 1000 KeV of $[DADPA]InBr_6 \cdot H_2O$, $[DADPA]InCl_6 \cdot H_2O$ and $[DADPA]In_{0.83}Sb_{0.17}Cl_6 \cdot H_2O$.

Table S1. Comparison of X-ray scintillation performance of organic-inorganic hybrid halides.

Materials	Grow method	Maximum emission (nm)	Light yield (photons/ MeV)	Detection limit (μGy/s)	Ref.
[DADPA]$In_{0.83}Sb_{0.17}Cl_6 \cdot H_2O$	**Solution method**	**552**	**51875**	**0.0983**	**This work**
$Cs_3Cu_2I_5$: single crystal	Bridgman method	500	51000	---	1
$(PPN)_2SbCl_5$	Antisolvent diffusion	635	49000	0.194	2
CsI(Na)	Non-vacuum crucible descent	420	41000	---	3
$[RQ]_2MnBr_4$	Solution method	530	34438	0.258	4
LYSO	Medium frequency induction heating	410	33000	---	5
$Cs_3Cu_2I_5$ single crystal	Bridgman method	440	32000	---	6
$CdWO_4$	Pulling method	480	28000	---	7
K_2CuBr_3 single crystal	Cooling method	391	23806	132.8	8
Ce:LuAG	Float-zone method	500	25000	---	9
[DADPA]$InCl_6 \cdot H_2O$	**Solution method**	**554**	**23054**	**---**	**This work**
$CsPbBr_3$ QDs	Single-step injection	520	21000	---	9
$(C_6H_5C_2H_4NH_3)_2Pb_{0.9}Sr_{0.1}Br_4 \cdot$single crystal	Antisolvent diffusion	440	19700	---	10
$(C_6H_5C_2H_4NH_3)_2Pb_{0.75}Ba_{0.25}Br_4 \cdot$single crystal	Antisolvent diffusion	440	19000	---	11
$MAPbBr_{0.05}Cl_{2.95} \cdot$single crystal	ITC method	420	18000	---	12
$CsPbCl_3$ single crystal	Bridgman method	440,600	1200	---	13

PPN = bis(triphenylphosphoranylidene)ammonium cation, [RQ] R = H, Me, Et, FEt, Q = quinuclidine.

Table S2. Crystal Data and Structural Refinements for compounds $[DADPA]InBr_6 \cdot H_2O$ and $[DADPA]InCl_6 \cdot H_2O$.

Compound	$[DADPA]InCl_6 \cdot H_2O$	$[DADPA]InBr_6 \cdot H_2O$
chemical formula	$C_6H_{22}N_3OInCl_6$	$C_6H_{22}N_3OInBr_6$
fw	479.78	746.54
Temp (K)	273	273.15
Space group	*P*-1	*P*-1
a (Å)	7.54750(10)	7.8936(3)
b (Å)	10.6805(10)	11.0840(5)
c (Å)	11.8682(2)	12.1633(5)
α (°)	94.6940(10)	94.554(2)
β (°)	107.997(2)	108.689(2)
γ (°)	109.4970(10)	109.0060(10)
V(Å^3)	839.27(2)	932.85(7)
Z	2	2
D_{calcd} (g·cm^{-3})	1.899	2.658
μ (mm^{-1})	19.974	14.108
F (000)	476	692
Reflections collected	17384	22852
Unique reflections	3389	5694
GOF on F^2	1.048	1.070
[a]R_1, wR_2 ($I > 2\sigma(I)$)	0.0231/0.0625	0.0311/0.0566
[b]R_1, wR_2 (all data)	0.0251/0.0632	0.0530/0.0619

[a]$R_1 = \sum||F_o| - |F_c||/\sum|F_o|$. [b]$wR_2 = [\sum w(F_o^2 - F_c^2)^2/\sum w(F_o^2)^2]^{1/2}$.

Table S3. Selected bond lengths (Å) and bond angles (°) for [DADPA]$InCl_6 \cdot H_2O$.

In1-Cl4	2.5034(5)	Cl6[1]-In1-Cl5[1]	91.958(18)
In1-Cl4[1]	2.5034(5)	Cl6-In1-Cl5[1]	88.042(18)
In1-Cl5[1]	2.5369(5)	Cl6[1]-In1-Cl5	88.042(18)
In1-Cl5	2.5369(5)	Cl6-In1-Cl5	91.958(18)
In1-Cl6	2.5341(5)	Cl1-In2-Cl2	90.349(19)
In1-Cl6[1]	2.5341(5)	Cl1[2]-In2-Cl2	89.651(19)
In2-Cl1	2.4888(5)	Cl1-In2-Cl2[2]	89.651(19)
In2-Cl1[2]	2.4888(5)	Cl1[2]-In2-Cl2[2]	90.349(19)
In2-Cl2[2]	2.5200(5)	Cl1[2]-In2-Cl3[2]	88.58(2)
In2-Cl2	2.5200(5)	Cl1-In2-Cl3	88.58(2)
In2-Cl3[2]	2.5319(5)	Cl1-In2-Cl3[2]	91.42(2)
In2-Cl3	2.5319(5)	Cl1[2]-In2-Cl3	91.41(2)
Cl4[1]-In1-Cl5	87.161(17)	Cl2-In2-Cl3	88.344(19)
Cl4-In1-Cl5[1]	87.161(17)	Cl2[2]-In2-Cl3	91.657(19)
Cl4-In1-Cl5	92.839(17)	Cl2[2]-In2-Cl3[2]	88.343(19)
Cl4[1]-In1-Cl5[1]	92.840(17)	Cl2-In2-Cl3[2]	91.656(19)
Cl4-In1-Cl6	88.847(18)	Cl4[1]-In1-Cl6	91.153(18)
Cl4-In1-Cl6[1]	91.153(18)	Cl4[1]-In1-Cl6[1]	88.847(18)

[1]-X,1-Y,1-Z; [2]2-X,2-Y,2-Z

Table S4. Hydrogen bonds data for [DADPA]$InCl_6 \cdot H_2O$.

D-H···A	d(D-H)	d(H···A)	d(D···A)	<(DHA)
N1-H1···Cl1	0.89	2.38	3.179(2)	149
N1-H1···Cl2	0.89	2.80	3.388(2)	125
N1-H2···Cl4	0.85	2.38	3.394(3)	143
N1-H3···Cl5	0.89	2.74	3.254(2)	167
N3-H11···O1	0.89	1.90	3.432(2)	135
N3-H13···Cl5	0.89	2.69	3.324(2)	174
N3-H13···Cl6	0.89	2.71	3.376(2)	129
N2-H19···Cl2	0.89	2.53	3.330(2)	133
N2-H20···Cl3	0.89	2.50	3.378(3)	150
N2-H21···Cl4	0.89	2.69	3.526(2)	170
O1-H24···Cl6	0.87(3)	2.83(3)	3.680(3)	167(3)
C2-H6···Cl4	0.97	2.81	3.771(3)	172
C4-H14···Cl2	0.97	2.72	3.496(2)	138

Table S5. Selected bond lengths (Å) and bond angles (°) for [DADPA]$InBr_6 \cdot H_2O$.

In1-Br1[1]	2.6590(4)	Br3-In1-Br3	91.822(12)
In1-Br1	2.6591(4)	Br5[2]-In2-Br4[2]	90.771(13)
In1-Br2	2.6914(4)	Br5-In2-Br4	89.229(13)
In1-Br2[1]	2.6913(4)	Br5-In2-Br4[2]	89.229(13)
In1-Br3[1]	2.6913(4)	Br5[2]-In2-Br4	90.771(13)
In1-Br3	2.6979(4)	Br5[2]-In2-Br6	88.821(12)
In2-Br4[2]	2.6970(4)	Br5-In2-Br6[2]	88.821(12)
In2-Br4	2.6970(4)	Br5[2]-In2-Br6	91.179(12)
In2-Br5	2.6410(4)	Br6[2]-In2-Br4	91.179(12)
In2-Br5[2]	2.6410(4)	Br6-In2-Br4[2]	91.967(12)
In2-Br6	2.6816(4)	Br6[2]-In2-Br4[2]	91.967(12)
In2-Br6[2]	2.6817(4)	Br6-In2-Br4	91.967(12)
Br1[1]-In1-Br1	89.059(12)	Br2[1]-In1-Br3	87.372(12)
Br1-In1-Br2[1]	89.060(12)	Br2-In1-Br3[1]	92.629(12)
Br1-In1-Br2	90.941(12)	Br2[1]-In1-Br2	92.628(12)
Br1[1]-In1-Br2[1]	90.941(13)	Br2-In1-Br3	87.372(12)
Br1[1]-In1-Br2	87.371(12)	Br2[1]-In1-Br3[1]	91.822(12)
Br1-In1-Br3	92.629(12)	Br1-In1-Br3[1]	92.628(12)

[1]-X,-Y,1-Z; [2]2-X,1-Y,2-Z

Table S6. Hydrogen bonds data for [DADPA]$InBr_6 \cdot H_2O$.

D-H···A	d(D-H)	d(H···A)	d(D···A)	<(DHA)
N1-H1···Br1	0.89	2.56	3.432(4)	167
N1-H2···Br3	0.89	2.87	3.573(3)	137
N1-H3···Br5	0.89	2.52	3.310(3)	14
N1-H3···Br6	0.89	2.91	3.480(3)	124
N2-H10···Br3	0.89	2.81	3.476(3)	133
N2-H10···Br2	0.89	2.84	3.492(3)	131
N2-H11···O1	0.89	1.90	2.785(6)	171
N3-H18··Br4	0.89	2.66	3.543(4)	169
N3-H20···Br6	0.89	2.70	3.478(4)	147
O1-H21···Br5	0.85	2.88	3.577(5)	140
O1-H22···Br3	0.88(6)	2.93(6)	3.540(5)	128(7)
C4-H13···Br6	0.97	2.83	3.603(4)	138

Reference

1. D. Yuan, *ACS Appl. Mater. Interfaces.* 2022, **12**, 38333-38340.
2. Q. He, C. Zhou, L. Xu, S. Lee, X. Lin, J. Neu, M. Worku, M. Chaaban, B. W. Ma, *ACS Mater. Lett.* 2020, **2**, 633-638.
3. G. F. Carpenter, M. J. Coe, A. R. Engel, *Nature*. 1976, **99**, 259.
4. J. Y. Li, C. F. Wang, H. D. Wu, L. Liu, Q. L. Xu, S. Y. Ye, L. Tong, X. Chen, Q. Gao, Y. L. Hou, F. M. Wang, J. Tang, L. Z. Chen, Y. Zhang, *Adv. Funct. Mater*. 2021, **31**, 2102848.
5. R. J. Sun, Z. F. Wang, H. Q. Wang, Z. H. Chen, Y. G. Yao, H. P. Zhang, Y. N. Gao, X. T. Hao, H. Q. Liu, Y. H. Zhang, *ACS Appl. Mater. Interfaces*. 2022, **14**, 36801-36806.
6. S. Cheng, A. Beitlerova, R. Kucerkova, M. Nikl, G. Ren, Y. Wu, *Phys. Status Solidi RRL*. 2020, **14**, 2000374.
7. A. G. Gandhi, H. H. Chiu, M. K. Ho, T. E. Hsu, T. Y. Li, Y. H. Wu, B. V. Kumar, P. M. Reddy, B. H. Lin, C. L. Cheng, S. Y. Wu, *ACS Appl. Nano Mater.* 2022, **5**, 14811-14823.
8. W. Gao, G. Niu, L. Yin, B. Yang, J. H. Yuan, D. Zhang, K. H. Xue, X. Miao, Q. Hu, X. Du, *ACS Appl. Electron. Mater.* 2020, **2**, 2242-2249.
9. Y. H. Zhang, R. J. Sun, X. Y. Ou, K. F. Fu, Q. S. Chen, Y. C. Ding, L. J. Xu, L. M. Liu, Y. Han, A. V. Malko, X. G. Liu, H. G. Yang, O. M. Bakr, H. Liu, O. F. Mohammed, *ACS Nano*. 2019, **13**, 2520-2525.
10. M. Akatsuka, N. Kawano, T. Kato, D. Nakauchi, G. Okada, N. Kawaguchi, T. Yanagida, *Nucl. Instrum. Methods Phys. Res., Sect. A.* 2020, **954**, 161372.
11. D. Nakauchi, N. Kawano, N. Kawaguchi, T. Yanagida, *Jpn. J. Appl. Phys.* 2020, **59**, SCCB04.
12. Q. Xu, W. Shao, J. Liu, Z. Zhu, X. Ouyang, J. Cai, B. Liu, B. Liang, Z. Wu, X. Ouyang, *ACS Appl. Mater. Interfaces.* 2019, **11**, 47485−47490.
13. K. Watanabe, M. Koshimizu, T. Yanagida, Y. Fujimoto, K. Asai, *Jpn. J. Appl. Phys.* 2016, **55**, 02BC20.